Spatial Symmetry Breaking Determines Spiral Wave Chirality

Thomas Quail, Alvin Shrier, and Leon Glass*
Department of Physiology, McGill University, Montreal, Canada H3G 1Y6
(Received 10 June 2014; revised manuscript received 31 July 2014; published 7 October 2014)

Chirality represents a fundamental property of spiral waves. Introducing obstacles into cardiac monolayers leads to the initiation of clockwise-rotating, counterclockwise-rotating, and pairs of spiral waves. Simulations show that the precise location of the obstacle and the pacing frequency determine spiral wave chirality. Instabilities predicted by curves relating the action potential duration and the pacing frequency at different spatial locations predict sites of wave break initiation and, hence, spiral wave chirality.

DOI: 10.1103/PhysRevLett.113.158101 PACS numbers: 87.19.Hh, 87.19.rp

Spiral waves, self-sustaining vortices of activity, have been observed in diverse biological and chemical contexts [1–3], and have been linked to mechanisms underlying various cardiac arrhythmias [4,5]. Chirality ("rotation direction") represents a fundamental property of spiral waves [6–10], and has recently been implicated in the dynamics of spiral wave anchoring to inexcitable obstacles [11]. The key factors regulating spiral wave chirality, however, remain unclear. A number of mechanisms have been implicated in spiral wave initiation [1,12–16]. Here, we investigate how inexcitable obstacles can lead to the initiation of spiral waves propagating in the tissue neighboring the obstacle [12,13]. To examine how the position of an inexcitable obstacle influences the chiral properties of these spiral waves, we introduced obstacles of varying sizes, approximately 1–8 mm in width, into cardiac monolayers (two of the preparations had two obstacles introduced).

We incubated 30 fertilized white leghorn chick eggs at 37 °C for 7–8 days [17]. We removed the ventricular portions of the embryonic hearts, dissociating the cells with trypsin. The cells were centrifuged, suspended in 818A medium [17], and plated in 10-mm-diameter circular glass rings on 35-mm-diameter plastic culture dishes. We incubated the cells for 48 h at 37 °C and 5% CO_2 during which time the monolayers formed—16 monolayers were included in the study. Thirty minutes prior to imaging, we loaded the cells with Calcium Green-1, a fluorescent dye that tracks intracellular calcium. The cells were imaged at between 35 °C–37°C using a custom-built macroscope with a 1 cm^2 field of view—we imaged the entire preparation (1-cm diameter). The system excites the calcium dye at 500 nm and monitors emission at 545 nm. The fluorescence was sampled at 40 Hz, with a spatial resolution of 80×80 pixels (0.15 μm^2). The dish was continuously perfused with fresh Hank's solution [17]. Side pacemakers emerged spontaneously with periods of 1–2 s. The wave front propagation velocity was approximately 4–5 mm/s. We introduced obstacles into the monolayers by surgical ablation. In particular, following the dye-loading incubation period, we made incisions into the monolayer using a fine x-acto blade, representing the approximate outline of a square, though due to the difficulty of the surgery some of the incisions were curvilinear. (In the two preparations with two obstacles, the obstacle shape was more circular.) We then excised the cells from within the outline of the obstacle. In some of the preparations, cell debris—and the associated calcium signal—became attached to the bottom of the dish in the obstacle area. This debris, however, was nonfunctional and did not influence the monolayer's dynamics. The approximate center of the obstacle was selected to be as close to the middle of the monolayer as possible. The fluorescent images were acquired using a Cardio-CCD camera with CARDIOPLEX software (Redshirt Imaging) approximately 3–5 min after the surgical ablation took place.

We observed a spectrum of spiral wave dynamics in the experimental recordings, including clockwise-rotating spiral waves (8), counterclockwise-rotating spiral waves (10), opposite-chirality pairs of spiral waves (4), a same-chirality clockwise-rotating pair of spiral waves (1), and same-chirality counterclockwise-rotating pairs of spiral waves (2). We determined the chirality through visual inspection. Transitions took place between spiral wave chiralities over the course of a single recording. In Fig. 1(a), two counter-rotating spiral waves govern the dynamics of a monolayer with an obstacle approximately 2 mm wide (see Supplemental Material, Movie 1 [18]). In Fig. 1(b), a counterclockwise-rotating spiral wave governs the dynamics of a monolayer with an obstacle approximately 5 mm in diameter (see Supplemental Material, Movie 2 [18]). Further, the positions of the obstacles are different: the approximate centroid of the obstacle in Fig. 1(a) is positioned down and to the left with respect to the centroid of the obstacle in Fig. 1(b).

The ubiquity of spiral waves observed in the experimental recordings led us to consider mechanisms of obstacle-induced spiral waves. Supplemental Fig. 1 [18]

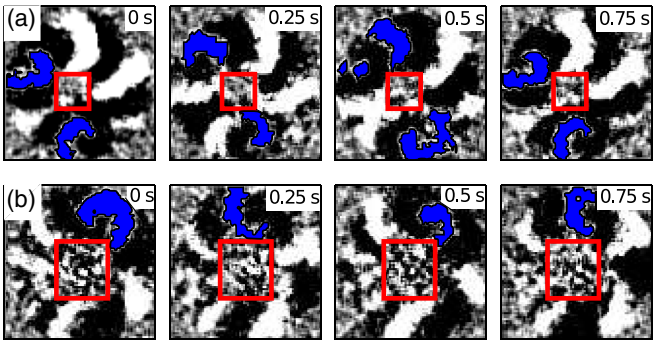

FIG. 1 (color online). Spiral wave propagation in cardiac monolayers composed of embryonic chick heart cells with inexcitable obstacles imaged using calcium-sensitive dyes. The red squares represent the position of the obstacles, the blue coloring represents the spiral waves, and the white coloring represents the waves emitted from the spiral waves. The diameter of the monolayer is 1 cm. (a) Two counterrotating spiral waves (at 10 and 6 o'clock) propagating in a cardiac monolayer with an obstacle width of 2 mm. The frames are separated by 0.25 s. (b) Counterclockwise-rotating spiral wave (at 1 o'clock) propagating in a cardiac monolayer with an obstacle width of 5 mm.

shows the initiation of an obstacle-induced spiral wave. We observed this transition in a 5-min recording in which a counterclockwise-rotating spiral wave on the left-hand side of the monolayer with a spiral period of approximately 0.55 s rapidly paced the tissue, initially generating wave fronts that propagated around a central obstacle that was positioned closer to the upper boundary, Supplemental Material, Fig. 1(a) [18]. Approximately 3.5 min later, waves emitted from the spiral wave detached from the obstacle, leading to the initiation of a counterclockwise-rotating spiral wave with a period of approximately 0.65 s, Supplemental Material, Fig. 1(b) [18]. (Supplemental Movies 3 and 4 display this transition.)

Theoretical studies have demonstrated that rapid side pacing of a sheet of cardiac tissue with an inexcitable and a partially excitable obstacle can lead to spiral wave initiation [12,13,19]. We investigated how the location of an obstacle with respect to a side pacemaker influenced the rotation direction of the initiated spiral waves using a highly simplified model of wave propagation through cardiac tissue based on the classic FitzHugh-Nagumo equations [20]:

$$\frac{\partial v}{\partial t} = \frac{1}{\epsilon}\left(v - \frac{v^3}{3} - w\right) + I_p + D\left(\frac{\partial^2 v}{\partial x^2} + \frac{\partial^2 v}{\partial y^2}\right), \quad (1)$$

$$\frac{\partial w}{\partial t} = \epsilon(v + \beta - \gamma w)g(v), \quad (2)$$

where $\epsilon = 0.42$, $\beta = 0.7$, and $\gamma = 0.5$. v represents the activation variable, the cells' transmembrane voltage, and w represents the tissue's recovery processes. We first tuned the parameters to locate a region in parameter space in which rapid side pacing would lead to spiral wave initiation. We then explored the range of the tissue's excitability parameter, ϵ, for which we could initiate spiral waves. Because cardiac monolayers composed of embryonic chick cells are slow conducting, we selected a larger value for ϵ. We integrated the equations using an Euler integration scheme with a $dt = 0.98$ msec (0.025 time units) and $dx = dy = 0.0083$ cm (0.025 space units) on a 1 cm $\times$ 1 cm grid. We scaled the arbitrary time and space units such that the dimensions of the system and the conduction velocity of propagating wave fronts were consistent with experiments. The diffusion coefficient is $D = 0.0028$ cm^2 s^{-1}. The boundary conditions along the edge of the square grid are no flux. We set $D = 0$ in the inexcitable obstacle, and in the tissue between the edge of the square grid and the monolayer's circular boundary. I_p and $g(v) = (w_h - w_p)/(1 + e^{-4v}) + w_p$ control the tissue's pacemaker properties. The periodic trajectory of the model can be split into four phases: the upstroke, the plateau, repolarization, and the pacemaker phase. w_p simply controls the rate of trajectory through the pacemaker phase. In the circular-shaped side pacemaker region (0.83 mm in diameter) located on the left-hand side of the sheet, $I_p = 1$, $w_h = 0.6$, and w_p is varied from between 0.15 to 0.66 to control the frequency. For the rest of the active cells, $I_p = 0$, $w_h = 0.6$, and $w_p = 0.4$. The sheet of tissue is isotropic, consistent with the lack of fiber orientation typically observed in monolayers. The obstacle is square shaped (2.5 mm in length) and is located in the center unless otherwise indicated.

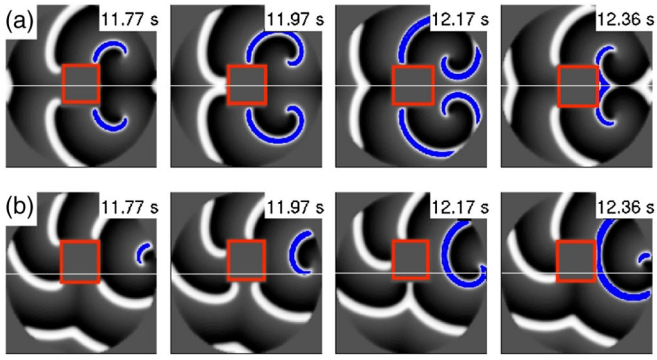

FIG. 2 (color online). Spiral wave propagation in a mathematical model of the experiments. The red squares represent the position of the obstacles, the blue coloring represents the spiral waves, and the white coloring represents the waves emitted from the spiral waves. The white line is the axis of symmetry between the pacemaker and the obstacle. (a) Two counterrotating spiral waves are initiated following rapid pacing at $T_p = 0.548$ s when the obstacle and the side pacemaker are symmetric. The times given in the top right of each panel represent the time following the cessation of rapid pacing. (b) A counterclockwise-rotating spiral wave is generated following rapid pacing ($T_p = 0.548$ s) when the obstacle is positioned upwards by 0.75 mm.

First, we considered the spatially symmetric system shown in Fig. 2(a). Figure 2(a) displays the steady-state dynamic following a 19.62 s burst of rapid pacing at a pacemaker period of $T_p = 0.548$ s, which gave rise to a pair of opposite-chirality spiral waves (the "time" given in the figure's panels is the time elapsed following the cessation of pacing). We broke the spatial symmetry by positioning the obstacle above the central axis of symmetry by 0.75 mm, Fig. 2(b), and pacing the tissue at the same period ($T_p = 0.548$ s), which led to the initiation of a counterclockwise-rotating spiral wave. Supplemental Material, Fig. 2 [18] shows the details of the initiation of the counterclockwise-rotating spiral wave during rapid pacing. The chirality of the initiated spiral wave observed numerically is consistent with the experimental trace in Supplemental Material Fig. 1 [18], in which an obstacle positioned closer to the upper boundary led to the initiation of a counterclockwise-rotating spiral wave following rapid pacing. Circular-shaped obstacles can also control chirality preference—Supplemental Fig. 3 [18] displays examples of this effect and further explanations.

Since frequency-dependent transitions are ubiquitous in the dynamics of cardiac systems [21], we examined how spiral wave dynamics changed as a function of side pacemaker period (T_p) when the obstacle was positioned above the central axis of symmetry by 0.75 mm. To mimic the experimental conditions, we introduced sparse randomly distributed heterogeneities ("breaks") into the medium by selecting a probability at each grid point of setting the diffusion coefficient equal to zero, $m_b = 0.000837$. Supplemental Material, Fig. 4 [18] details how m_b influences spiral wave chirality.

We generated 20 substrates, simulating each substrate through a range of T_p, Fig. 3. For each T_p value, using visual inspection, we classified the dynamics (following 100 000 iterations corresponding to approximately 1.5 min in the experimental system) into four behaviors: clockwise-rotating spirals, counterclockwise-rotating spirals, no spiral formation, and others, which included pairs of spiral waves of the same or opposite chirality, and groups of 3 or more spiral waves. Then we computed the moving average of the fraction f of the experiments (out of 20) that displayed each specific spiral wave behavior, as shown in Fig. 3 and Supplemental Material, Fig. 5 [18]. We averaged the corresponding f values over two T_p discretizations (totaling 0.002 s) to smooth out short-term noise-induced fluctuations.

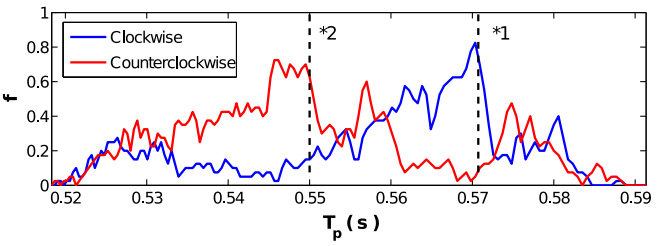

FIG. 3 (color online). Spiral wave chirality as a function of the pacemaker period (T_p). **f** represents the moving average of the fraction out of 20 from each category that was observed at each value of T_p. The obstacle was positioned above the central axis of symmetry by 0.75 mm for all simulations. *1 represents the T_p at which the map derived from the action potential duration restitution curve above the obstacle destabilized. *2 represents the T_p at which the map from below the obstacle destabilized.

At T_p values > 0.59 s, spiral waves did not form because the substrate supported the stable propagation of waves through the system. Second, at *1 in Fig. 3, the region above the obstacle destabilized, leading to the initiation of predominantly clockwise-rotating spiral waves (typically forming above the obstacle). Third, at *2 in Fig. 3, the region below the obstacle destabilized, leading to the initiation of predominantly counterclockwise-rotating spiral waves. Lastly, for short T_p values, the pacemaker transitioned from 1:1 propagation (in which 1 pulse propagates away from the side pacemaker region for every stimulus) to 3:2 propagation (in which 2 pulses propagate away from the side pacemaker for every three stimuli) and spiral wave formation was infrequent.

Spiral wave initiation takes place in a region of the substrate following an instability that leads to propagation block. Action potential duration (APD) restitution curves predict the onset of instabilities in excitable media [22–24]. We computed steady-state APD restitution curves at positions both above and below the obstacle (see Supplemental Material, Fig. 2 [18] for the precise locations) by varying w_p, the parameter controlling the pacemaker period. Both spatial locations are 0.75 mm from the left edge of the obstacle and 0.17 mm above or below the obstacle. We considered the duration of the action potential to be the time that v is greater than -0.5. Supplemental Fig. 6 [18] is a representative v waveform displaying the threshold and characteristic shape of the time series. We fit the steepest portions of the curves only to maximize the precision of the pacing period at which these maps destabilized. We fit the following exponential to both of the restitution curves: $f(\rho) = \alpha e^{\eta(\rho-\delta)} + \Gamma$ where for the curve computed *above* the obstacle: $\alpha = -0.89$, $\eta = -5.32$, $\delta = 11.06$, and $\Gamma = 3.34$—and for the curve computed *below* the obstacle: $\alpha = -0.51$, $\eta = -5.74$, $\delta = 10.80$, and $\Gamma = 3.26$. The output from these curves was in time units (t.u.). To convert to seconds, we applied the time scale factor: 1 t.u. $= 0.0392$ s. The morphology of the restitution curves along the top and bottom edges of the obstacle change due to the interactions of the curved wave front with the obstacle. However, given two restitution curves the same distance along both the top and bottom edge (with the same threshold), the restitution curve along the top of the obstacle becomes steeper before the restitution curve along the bottom of the obstacle because the wave front curvature is greater along the top edge.

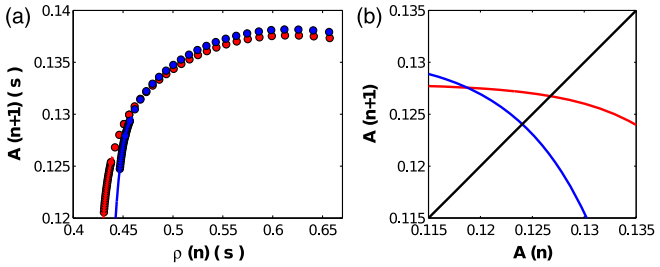

FIG. 4 (color online). Instabilities in the APD restitution curves at different spatial locations are consistent with the change in spiral wave chirality observed in Fig. 3. (a) APD is computed as a function of recovery time, $\rho(n)$, both above (blue) and below (red) the obstacle. The dots represent the steady-state APD computed numerically. The lines represent a nonlinear-least-squares regression fit to an exponential. (b) One-dimensional maps of APD at $T_p = 0.57$ s are derived from the restitution curves computed both above (blue) and below (red) the obstacle. At $T_p = 0.57$ s, the dynamics below the obstacle are stable because the absolute value of the slope through the fixed point is < 1, and the dynamics above the obstacle are unstable because the absolute value of the slope through the fixed point is > 1.

We plotted the corresponding APD restitution curves in Fig. 4(a), where the blue curve corresponds with the location above the obstacle, and the red curve corresponds with the location below the obstacle. To compute the T_p at which these maps destabilized, we assume that

$$T_p = A(n) + \rho(n), \tag{3}$$

where the pacemaker period is equal to the duration of the action potential plus the recovery time. We also assume that $A(n+1) = f(\rho(n))$—that is, the duration of the 'next' action potential, $A(n+1)$, is a function of the amount of time the cell has had to recover, $\rho(n)$. By rearranging Eq. (3), we derive the following one-dimensional map: $A(n+1) = f(T_p - A(n))$, which has a unique fixed point that destabilizes at a particular T_p value, Fig. 4(b). The map derived from the dynamics of the region above the obstacle (blue curve) destabilizes at $T_p = 0.57$ s, which corresponds with *1 in Fig. 3, predicting the increase in the clockwise-rotating spirals. The map derived from the region below the obstacle (red curve) destabilizes at $T_p = 0.55$ s, which corresponds with *2 in Fig. 3, predicting the increase in the counterclockwise-rotating spirals. Both T_p values predicted by the maps computed at these spatial locations are consistent with the pacemaker periods at which both regions destabilized, and thus are predictive of the increases in the number of clockwise-rotating and counterclockwise-rotating spiral waves as a function of T_p.

Although spiral waves propagating in excitable media are believed to play an important role in the genesis of many serious cardiac arrhythmias, not much attention has focused on the chiral nature of spiral waves. However, in medicine, the chirality of one arrhythmia, atrial flutter, is clinically relevant, and the direction of circulation of excitation waves in the right atrium is typically classified as either clockwise or counterclockwise [25].

Here, we discovered that an asymmetry in the position of an obstacle with respect to a position of a pacing site in combination with the side pacing frequency determines spiral wave chirality for an isotropic cardiac medium. Recently, Gizzi *et al.* demonstrated that the location of the pacing site gave rise to differences in the patterns of alternans observed in the right ventricles of canines [21]. Gizzi *et al.* also claimed that the intrinsic heterogeneities of the right ventricle accounted for the differences [21], which is consistent with the findings of our study. Studies have also addressed the role of obstacle shape in the context of electric-field-induced wave source initiation [26–28]. This study opens up many future research directions, including how obstacle size, obstacle shape, model parameters controlling tissue excitability, and fiber orientation influence spiral wave chirality preference. Hörning recently showed that fiber orientation greatly influences the unpinning properties of spiral waves attached to obstacles [29]. Our examination of the symmetry breaking properties and instabilities of this simplified cardiac system provide another example in which the geometry of the substrate plays a critical role in the determination of the system's asymptotic dynamics.

This work was supported by Grants from NSERC, CIHR, and HSF of Canada. The experiments were carried out in accordance with ethical standards, and approval was received from the Environmental Health and Safety at McGill University.

*glass@cnd.mcgill.ca

[1] J. M. Davidenko, A. V. Pertsov, R. Salomonsz, W. Baxter, and J. Jalife, Nature (London) **355**, 349 (1992).
[2] E. Pálsson and E. C. Cox, Proc. Natl. Acad. Sci. U.S.A. **93**, 1151 (1996).
[3] X. Huang, W. Xu, J. Liang, K. Takagaki, X. Gao, and J.-Y. Wu, Neuron **68**, 978 (2010).
[4] S. M. Narayan, D. E. Krummen, K. Shivkumar, P. Clopton, W.-J. Rappel, and J. M. Miller, J. Am. Coll. Cardiol. **60**, 628 (2012).
[5] T. Ikeda, M. Yashima, T. Uchida, D. Hough, M. C. Fishbein, W. J. Mandel, P.-S. Chen, and H. S. Karagueuzian, Circ. Res. **81**, 753 (1997).
[6] R. M. Zaritski and A. M. Pertsov, Phys. Rev. E **66**, 066120 (2002).
[7] C. Zemlin, K. Mukund, M. Wellner, R. Zaritsky, and A. Pertsov, Phys. Rev. Lett. **95**, 098302 (2005).
[8] C. W. Zemlin, K. Mukund, V. N. Biktashev, and A. M. Pertsov, Phys. Rev. E **74**, 016207 (2006).
[9] O. Steinbock, J. Schütze, and S. C. Müller, Phys. Rev. Lett. **68**, 248 (1992).

[10] K. Agladze and P. De Kepper, J. Phys. Chem. **96**, 5239 (1992).
[11] C. W. Zemlin and A. M. Pertsov, Phys. Rev. Lett. **109**, 038303 (2012).
[12] A. V. Panfilov and J. P. Keener, J. Theor. Biol. **163**, 439 (1993).
[13] A. Xu and M. R. Guevara, Chaos **8**, 157 (1998).
[14] G. Bub, A. Shrier, and L. Glass, Phys. Rev. Lett. **88**, 058101 (2002).
[15] L. D. Weise and A. V. Panfilov, Phys. Rev. Lett. **108**, 228104 (2012).
[16] S. Alonso and M. Bär, Phys. Rev. Lett. **110**, 158101 (2013).
[17] R. L. DeHaan, Dev. Biol. **16**, 216 (1967).
[18] See Supplemental Material at http://link.aps.org/supplemental/10.1103/PhysRevLett.113.158101 for movies of spiral waves propagating in cardiac monolayers, more information on obstacle-induced spiral wave formation following rapid pacing, and additional details on how obstacle geometry and heterogeneities influence spiral wave chirality preference.
[19] Y. Biton, A. Rabinovitch, I. Aviram, and D. Braunstein, Phys. Lett. A **373**, 1762 (2009).
[20] K. Hall and L. Glass, Phys. Rev. Lett. **82**, 5164 (1999).
[21] A. Gizzi, E. M. Cherry, R. F. Gilmour, Jr., S. Luther, S. Filippi, and F. H. Fenton, Front. Phys. **4**, 71 (2013).
[22] M. Guevara, G. Ward, A. Shrier, and L. Glass, IEEE Comp. Cardiol. **562**, 167 (1984).
[23] B. Echebarria and A. Karma, Phys. Rev. Lett. **88**, 208101 (2002).
[24] T. Krogh-Madsen and D. J. Christini, Biophys. J. **92**, 1138 (2007).
[25] N. Saoudi, F. Cosío, A. Waldo, S. A. Chen, Y. Iesaka, M. Lesh, S. Saksena, J. Salerno, and W. Schoels, Eur. Heart J. **22**, 1162 (2001).
[26] V. G. Fast, S. Rohr, A. M. Gillis, and A. G. Kléber, Circ. Res. **82**, 375 (1998).
[27] A. Pumir, V. Nikolski, M. Hörning, A. Isomura, K. Agladze, K. Yoshikawa, R. Gilmour, E. Bodenschatz, and V. Krinsky, Phys. Rev. Lett. **99**, 208101 (2007).
[28] P. Bittihn, M. Hörning, and S. Luther, Phys. Rev. Lett. **109**, 118106 (2012).
[29] M. Hörning, Phys. Rev. E **86**, 031912 (2012).